Journal of
Materials Chemistry C

ROYAL SOCIETY
OF CHEMISTRY

PAPER

View Article Online
View Journal

Check for updates

Cite this: DOI: 10.1039/d5tc04167h

Extreme ultraviolet induced reactions of tin–oxo cage photoresists

Najmeh Sadegh,†[a] Jarich Haitjema, †[a] Yu Zhang,[a] Lianjia Wu,[a] Olivier Lugier, [a] Ivan Bespalov, [a] Dimitrios Kazazis, [b] Michaela Vockenhuber,[b] Yasin Ekinci,[b] Katharina Witte,[b] Benjamin Watts, [b] Ivan Pollentier,[c] Danilo De Simone [c] and Albert M. Brouwer *[ad]

Received 25th November 2025,
Accepted 5th February 2026

DOI: 10.1039/d5tc04167h

rsc.li/materials-c

The performance of photoresists is a major challenge in extreme ultraviolet (EUV) lithography and needs to be improved for the future technology nodes that require higher resolution, patterning fidelity, and sensitivity. Hybrid inorganic/organic materials are considered for this crucial function, but the chemical mechanisms underlying their solubility switching are not well understood, which hampers the rational improvement of EUV photoresists. Here we study *n*-butyltin–oxo cages, a readily accessible "open source" representative negative tone resist. Upon exposure to EUV radiation (wavelength 13.5 nm), butane, butene and octane are the main volatile reaction products. Tin is fully retained in the films even after prolonged EUV exposure. It is found that the loss of only ~18% of the butyl groups suffices to render the resist film insoluble. The initial quantum efficiency of Sn–C bond cleavage is $\Phi \approx 5$ per absorbed EUV photon, but this decreases rapidly with conversion of the material. After the primary Sn–C bond cleavage in a tin–oxo cage, induced by photoionization or capture of a (secondary) photoelectron, facile thermal reaction steps may occur that lead to additional Sn–C bond breaking. Although many questions remain, our work sheds new light on the reaction mechanisms at play and provides input for simulations of the lithographic process.

Introduction

The roadmap of the semiconductor industry dictates a continuous shrinkage of the smallest features of computer chips.[1] For high-volume manufacturing, extreme ultraviolet lithography (EUVL) has been introduced, because its short wavelength (λ = 13.5 nm) increases the optical resolution and allows to write very small patterns with a single exposure. On the instrumental side, engineering and physics drive the continuous progress of EUV source power, mask performance, and numerical aperture.[2–4] Another important factor in lithography is the photoresist, which translates the aerial image to a physical pattern on the substrate, using a chemical process that switches the solubility so that either the exposed or the unexposed parts of the resist film are dissolved in a developer liquid, giving rise to positive and negative tone resists, respectively.

Photoresists are typically molecular or low-molecular-weight polymer materials. They face stringent requirements on resolution, line edge roughness, and sensitivity,[5] but it is difficult to rationally improve their performance because the understanding of the molecular chemistry induced by EUV photons is still limited. When an EUV photon (energy 92 eV) is absorbed by a material, it induces ejection of an electron from a molecular orbital or from a relatively shallow atomic core level.[6] The primary electron generated loses its energy by inelastic scattering events, generating several secondary electrons.[7] EUV chemistry is often described as electron-induced chemistry.[8] However, for every electron generated, a hole is also produced, and depending on the chemical system, both holes and electrons (after losing most of their excess energy) can be reactive species. Moreover, in the energy loss process, electronically excited states can be generated (as in UV photochemistry) and a substantial amount of heat is released. Thus, multiple reactions per absorbed photon are possible, giving rise to a potentially high photochemical quantum yield. For example, it has been reported that photoacid generators, which are the key elements in chemically amplified photoresists (CARs) for ultraviolet lithography,[9–11] can generate up to 13 protons per absorbed EUV photon.[12–14] On the other hand, recombination processes of electrons and holes or radicals formed by homolytic bond cleavage can occur, reducing the net reactivity.

---

[a] *Advanced Research Center for Nanolithography, P.O. Box 93019, 1090 BA Amsterdam, The Netherlands*
[b] *PSI Center for Photon Science, Paul Scherrer Institut, Villigen 5232, Switzerland*
[c] *Imec, Kapeldreef 75, B3001 Leuven, Belgium*
[d] *University of Amsterdam, van't Hoff Institute for Molecular Sciences, P.O. Box 94157, 1090 GD Amsterdam, The Netherlands. E-mail: A.M.Brouwer@uva.nl*

† These authors made equal contributions.

Many materials are being considered as potential resists for EUVL for future technology nodes.[15–25] The industry naturally adapted the well-understood chemically amplified resists (CARs) based on photoacid generation to the new EUVL application.[1] However, these organic materials have reduced sensitivity because they do not absorb EUV photons efficiently and they exhibit low etch resistance.[26] This becomes more important in the advanced technology nodes because the thickness of resist films has to be decreased to avoid high aspect ratios which lead to the risk of pattern collapse and to match the decreasing depth of focus with the increase of the numerical aperture of the EUV illumination system. Organometallic compounds can absorb EUV radiation more strongly and due to their higher density can provide higher etch resistance, which makes them suitable hard masks for pattern transfer. Tin–oxo cages, introduced to the field by the Brainard group, are a popular type of metal–organic resist.[27–32] Two representative tin–oxo cages with different counterions, nicknamed TinOH and TinF, are studied in the present work (Chart 1). The presence of tin is beneficial for resist sensitivity, because it gives rise to strong absorption of EUV photons. The absorption coefficient α was found to be $\sim 12\ \mu\text{m}^{-1}$ for a number of *n*-butyltin–oxo cages with different counterions.[33] This is much larger than for most organic materials ($\alpha < 5\ \mu\text{m}^{-1}$),[26] yet still smaller than for the tin-containing resists developed by Inpria (α up to $\sim 20\ \mu\text{m}^{-1}$).[33]

As stated above, not much is known in molecular detail about the chemical reaction mechanism of EUV photoresists.[34–40] This is partly due to the lack of powerful analytical tools that can give relevant spectroscopic information on the very small amounts of material in thin films. To aggravate this challenge, for a good mechanistic understanding, the initial reaction products should be detected separately from follow-up products, which requires measurements at small conversion. Infrared spectroscopy is moderately sensitive, but feasible and useful when changes of characteristic functional groups can be observed.[35,40–42] X-ray photoelectron spectroscopy (XPS) is extremely sensitive, but the changes in the binding energies of the different atoms are not always large and it can be difficult to interpret the spectra in terms of molecular structures.[29,34,42–45] A more straightforward use of XPS is the determination of the elemental composition of the thin film. In the case of the tin–oxo cages the loss of carbon is readily monitored using the relative strength of the carbon 1s signal. The surface sensitivity of XPS can be a benefit, but also a disadvantage, because XPS does not monitor the resist film throughout its depth, and surface contamination is a persistent concern.

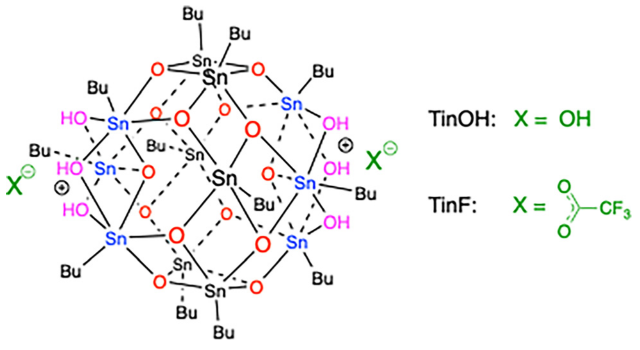

Chart 1 Compounds investigated.

In the present work, we use X-ray absorption spectroscopy, measured in transmission mode and therefore not surface-specific, to analyze the chemical composition of photoresist films before and after EUV exposure. In addition, we perform experiments with a tool that allows measurement of volatile reaction products by means of mass spectrometry and determination of the film thickness at the same location using ellipsometry before exposure, after exposure, and after development. Using the measured shrinkage of the film, we estimate the quantum yield of the fundamental reaction: tin–carbon bond cleavage. Taking the outgassing products into account, we discuss the current understanding of the working mechanism of tin–oxo cages as a negative tone EUV resist.

Simulation models for EUV pattern formation have been reported that use building blocks resembling tin–oxo cages.[46–52] These models are calibrated using limited experimental data obtained with materials of unknown structure. The present work provides experimental data on a well characterized "open-source" material, and this can contribute to the further understanding of the pattern formation process in EUV lithography.

Experimental

Materials

Synthesis of the tin–oxo cage materials was performed as in earlier work, following well-known literature procedures.[53–55] Preparation of thin films by spin coating is described in detail in the SI.

EUV exposures

Thin films on SiN membranes (3×3 mm^2) supported by a 7.5×7.5 mm^2 Si frame were exposed to EUV synchrotron radiation at 92 eV at the XIL-II beamline of the Paul Scherrer Institute.[56] Areas of $500 \times 500\ \mu\text{m}^2$ were irradiated homogeneously with different doses in different parts of the membrane. A part of the samples was developed in isopropanol/water 2 : 1 for 30 seconds and rinsed with demineralized water to remove unexposed material. The thickness of the films was measured using atomic force microscopy (AFM), using a Bruker Dimension Icon AFM, operating in tapping mode, using Bruker OLTESPA AFM probes with a frequency between 70 and 80 kHz. 512 samples per line were recorded on areas of approximately $20 \times 20\ \mu\text{m}^2$ using an operating speed of 1 Hz.

X-ray transmission measurements

The scanning transmission X-ray microscope at the PolLux beamline at the Paul Scherrer Institute[57] was used to record soft X-ray absorption spectra and absorption images at selected energies as described in detail in the SI.

Outgassing experiments

A set-up at imec was used to irradiate thin films of TinOH and TinF on silicon wafers with 13.5 nm radiation obtained from an Energetic EUV source.[58] Gaseous products were detected using a residual gas analyzer while the wafer was scanned at a constant speed. The mass spectra of the product mixtures (up to $m/z = 300$) were compared with the reference spectra (NIST) of *n*-butane, 1-butene, carbon dioxide and *n*-octane to estimate the product distribution. In addition, time traces with exposure at a single spot were recorded for selected masses. The same exposure tool was used to irradiate areas on the sample with different doses, and the thickness of the film was measured using ellipsometry both before and after development.

Additional experimental details are provided in the SI.

Results and discussion

X-ray transmission measurements

Soft X-ray absorption spectroscopy provides information about the chemical composition of the photoresist film by measuring absorbance at energies well above an absorption edge, where the spectrum is devoid of fine structure and the absorption coefficients can be predicted using tabulated atomic cross sections.[59]

In previous work, we reported the X-ray absorption spectra of TinOH and TinF at the C and O K-edges.[60] Here we focus on 320 and 515 eV as energies where mainly carbon and tin absorb, respectively, and 550 eV, where both tin and oxygen have strong absorption. By combining the absorbance at these three energies the ratios of the three elements can be derived. Since hydrogen absorbs X-rays very weakly, its absorption was neglected if the amount of hydrogen was unknown (*e.g.* exposed tin–oxo cage films) or calculated using the molecular formula (PMMA and PS reference samples, unexposed tin–oxo cage films). Absorption from fluorine was approximated using the molecular formula of TinF (unexposed TinF samples). Fluorine was estimated to contribute at most 2% to the total absorption at 320 eV in TinF, which means that its influence on the results is small. For EUV-exposed TinF samples, the fluorine absorption was neglected because the elemental composition after exposure is unknown. This may lead to a small overestimation of the amount of carbon (<3%), while the effect on other elemental quantities is negligible.

Images were recorded with a scanning transmission X-ray microscope (STXM) that covered both exposed and unexposed regions of the tin–oxo cage films. Unexposed parts of the resist film were cleared by development (negative tone), leaving a bare membrane in the unexposed region. The transmitted intensity through the tin–oxo cage film (I) and the intensity through the bare membrane (I_0) can be calculated by selecting parts of the raster and averaging the counts in each area. An example is shown in Fig. 1. The exposed part is darker because it contains an X-ray absorbing film.

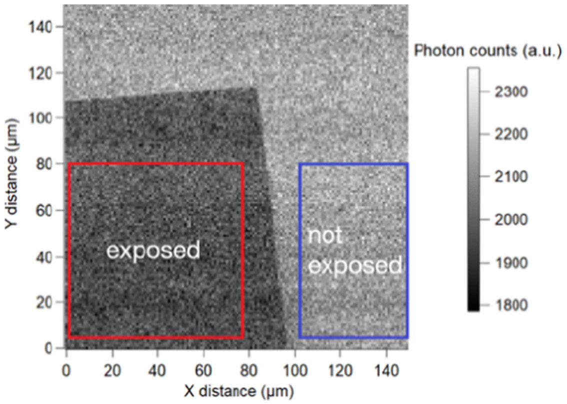

Fig. 1 X-ray transmission image (photon energy 550 eV) of a TinOH thin film spin-coated on top of a SiNx membrane, partially exposed by EUV light (100 mJ cm^{-2}) and developed to remove unexposed material.

The absorbance A is calculated from the average intensities of the transmitted X-rays $\bar{I}$ and $\bar{I}_0$ in the two areas according to eqn (1). At each energy E, the absorbance (neglecting the contribution of hydrogen and fluorine) is given by eqn (2). The products of the elemental concentrations c_i and atomic cross sections σ_i are the elemental surface densities S_i (mol cm^{-2}).

$$A = -\ln(\bar{I}/\bar{I}_0) \quad (1)$$

$$A_E = \alpha_E \cdot d = (c_C\sigma_{C(E)} + c_O\sigma_{O(E)} + c_{Sn(E)}\sigma_{Sn(E)}) \cdot d \quad (2)$$

By measuring the absorbance at three different energies, we obtain three equations from which the three unknown surface densities can be derived, as described in the SI. When the thickness d is not known, we only calculate the ratios of the concentrations of the three elements c_C, c_O, and c_{Sn}. The atomic cross sections σ_C, σ_O and σ_{Sn} were initially taken from the CXRO database.[61] Because we found that the concentration of oxygen in the pristine TinOH film was overestimated, we performed reference measurements using samples of polystyrene, polymethyl methacrylate and tin, and re-derived the cross sections at the energies of interest. Details are given in the SI. The cross sections (Table S1) for C and Sn match well with the tabulated ones, and those of O differ a bit more, but are rather uncertain because of the relatively small amount of O in the reference material. The experimental compositions of thin films of TinOH and TinF based on the adjusted cross sections are compared with the theoretical ones based on the chemical composition in Fig. 2.

For TinOH, an excellent agreement is found. For TinF, the carbon content is overestimated relative to that of tin, and the oxygen content is underestimated. Clearly, the statistical error bars derived from the intensities of the transmitted light do not capture all uncertainties in the experimental data. The measurements at different energies are performed at different locations on the sample to minimize the effects of radiation damage. Differences in the thickness at different locations on the membrane therefore contribute to the uncertainties. The largest errors are for oxygen because this has a relatively small cross section at all available photon energies (Table S1). The limited amount of available data does not allow us to assess the uncertainties quantitatively. As will be shown below, however,

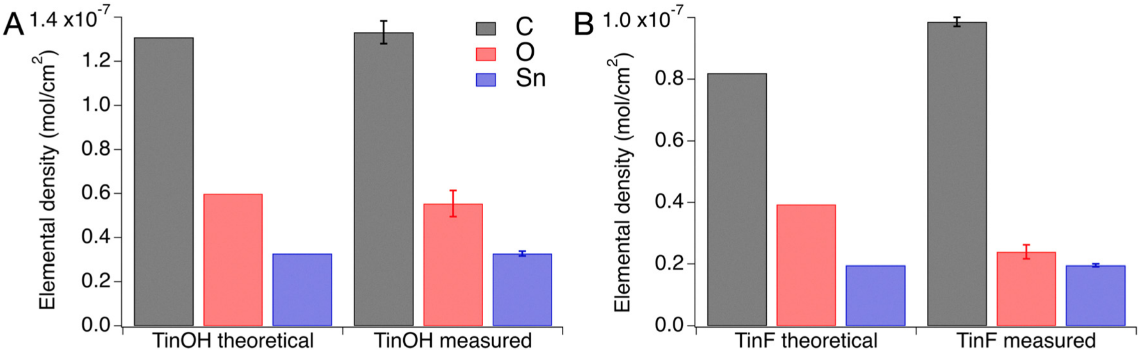

Fig. 2 Theoretical and experimental compositions of thin films of (A) TinOH ($C_{48}H_{116}O_{22}Sn_{12}$) and (B) TinF ($C_{52}H_{114}O_{24}Sn_{12}F_6$). Error bars are based on the standard error of the mean (SEM) of the measured transmission. The amount of tin in the theoretical and experimental compositions was assumed to be identical.

clear and consistent trends can be discerned in the data from EUV exposure experiments.

We apply the method of analysis to films of TinOH and TinF exposed to EUV radiation and subsequently developed (as exemplified in Fig. 1), and to films that were exposed but not developed. In the latter case, we measured the absorption difference between exposed and unexposed areas.

A spin-coated film of TinOH was exposed to EUV light with four different doses: 50 mJ cm^{-2}, 100 mJ cm^{-2}, 200 mJ cm^{-2}, and 500 mJ cm^{-2}. STXM raster scans were recorded (320, 515 and 550 eV) at the edges of exposed areas. The resulting absorption values were converted to elemental compositions using eqn (S3). The results are shown in Fig. 3 for samples that were developed after exposure.

The most conspicuous trend in the data is the decrease of the amount of carbon detected with increasing exposure. When comparing the four exposed samples in Fig. 3, we can conclude that within the limits of the accuracy of the measurements, oxygen (standard deviation 12%) and tin (standard deviation 7%) remain in the resist film. In earlier studies of the photoconversion of tin–oxo cages we have assumed that tin is not lost from the film during exposure,[29,62] and the present data justify this assumption. In agreement with the results of the film thickness measurements discussed below, the lowest dose of 50 mJ cm^{-2} already causes almost complete conversion of TinOH to insoluble products, and development does not remove appreciable amounts of soluble tin–oxo cage materials.

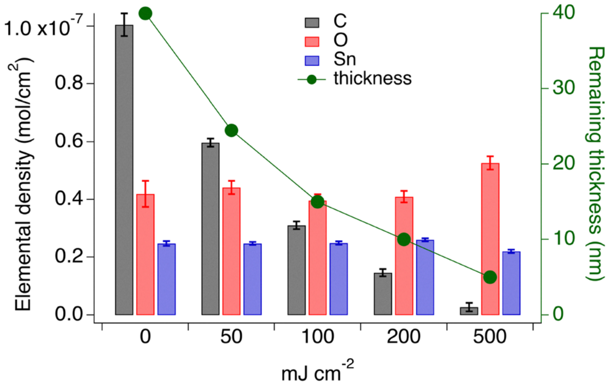

Fig. 3 Measured elemental composition of EUV-exposed and developed TinOH films (bars, left axis) and remaining film thickness (green markers, right axis). The unexposed film was not developed; its composition was normalized to the amount of tin in the 50 mJ cm^{-2} exposed material. The surface density corresponds to an initial thickness of ~40 nm.[62] For the developed samples, the thickness was measured using AFM.

The elemental composition of TinF films after exposure and development is shown in Fig. 4A. As compared to TinOH (Fig. 3), the results are quite different. A clear loss of all three elements is apparent at the low doses of 50 and 100 mJ cm^{-2}. This is attributed to removal of unreacted or insufficiently converted material by the developer. Clearly, the solubility switch requires a higher dose for TinF than for TinOH. At high doses, almost all material is converted to insoluble compounds, and the remaining amount of tin and oxygen is higher than for low doses. Very little material remains at low doses, as can be seen from both the thickness and the elemental composition measurements. The amount of carbon first decreases strongly (because the development process removes most of the film), then increases at 100 mJ cm^{-2} (because more resist material has become insoluble) and decreases again at 500 mJ cm^{-2} because of further outgassing of carbon-containing species. The amounts of O and Sn are smaller at a dose of 100 mJ cm^{-2} than at 500 mJ cm^{-2}, indicating that development still removed the material. For TinF, a dose >100 mJ cm^{-2} is required for reaching the maximum film retention, while for TinOH, ~50 mJ cm^{-2} is sufficient. The study of the volatile reaction products below shows a 2× smaller outgassing rate for TinF, consistent with the observed smaller sensitivity.

For samples that are exposed but not developed, the measurement of the transmission in the exposed and unexposed areas gives the absorption differences with respect to the unexposed material, and the AFM experiments measure the shrinkage of the film (Fig. 4B). Absorption changes, resulting only from outgassing of volatile products, show a clear decrease in the amount of carbon. For the dose of 50 mJ cm^{-2}, no accurate ΔA and thickness data could be obtained because the contrast was too low. Outgassing of tin and oxygen is clearly not important, since the ΔS values are very close to zero.

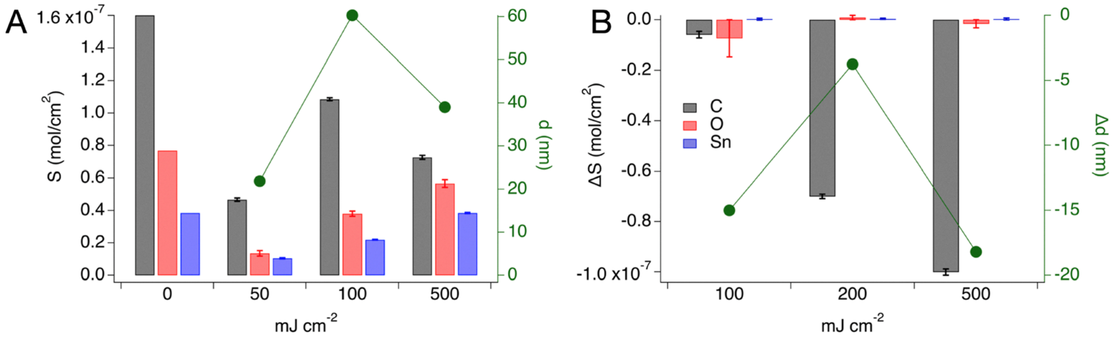

Fig. 4 Analysis of TinF films exposed to EUV. (A) Thickness (*d*) and elemental surface densities (*S*) after exposure and development. (B) Change of thickness and elemental densities due to exposure without development.

This agrees with the result for TinOH (Fig. 3) and with the outgassing experiments described in the next section.

Volatile reaction products

The loss of carbon-containing volatile reaction products as a result of breaking of tin–carbon bonds is a well-known characteristic of the photochemistry and radiation chemistry of tin–oxo cages.[28–30,39,63–66] In the present work we directly and semi-quantitatively identify the reaction products by means of mass spectrometry. Films of TinOH and TinF on silicon wafers were irradiated at 13.5 nm and the volatile reaction products analyzed using a residual gas analyzer (RGA). During the irradiation the sample was moved at constant speed, resulting in an average dose of ∼30 mJ cm^{-2} over the irradiated area. Mass spectra are recorded during the scan in 11 time intervals of ∼2 minutes, in the range of 0–300 amu. After subtraction of the background recorded under the same conditions, but without resist material on the Si wafer, mass spectra of the reaction mixture are obtained. A representative mass spectrum of the outgassing products of TinOH averaged over the 11 acquisitions during one run is shown in Fig. 5A. Spectra of all three samples studied are shown in the SI (Fig. S7).

The spectra show characteristic molecular ion peaks of octane (m/z 114), butane (m/z 58) and butene (m/z 56), as well as a small amount of carbon dioxide (m/z 44). There are no significant product signals at $m/z > 120$, which excludes the presence of low molecular weight tin compounds, in line with the STXM results. The spectrum of TinF (Fig. S7) shows small peaks (not present in the spectra of TinOH) at 69 amu (CF_3^+) and 19 amu (F^+) indicating decomposition of the counterion. The reported mass spectrum of CF_3COOH shows a strong peak at 45 amu,[67] but this is not observed in the spectrum of TinF, so proton transfer to the counterion and outgassing of the neutral acid do not occur, in contrast to what was recently reported for the more basic acetate and pivalate analogs.[68]

To estimate the contributions of the different products, the spectra are compared with the reference spectra of *n*-octane, *n*-butane, 1-butene and carbon dioxide from the NIST database,[67,69] as described in detail in the SI. We studied samples of TinOH and TinF under the same conditions and later repeated the experiment with a different batch of TinOH (run 2). The outgassing rates of the products derived from TinOH during an experiment involving 11 subsequent measurements are shown in Fig. 5B. The average yields of the products are listed in Table 1.

As shown in Fig. S7 (SI), after fitting the total mass spectrum as a sum of the four reaction products, a part of the total peak intensity remains unaccounted for, mostly in the low m/z range. One possible cause is the presence of small quantities of unidentified low molecular weight outgassing products. Another important factor is the potential mismatch between the reference spectra from the NIST database and the measured

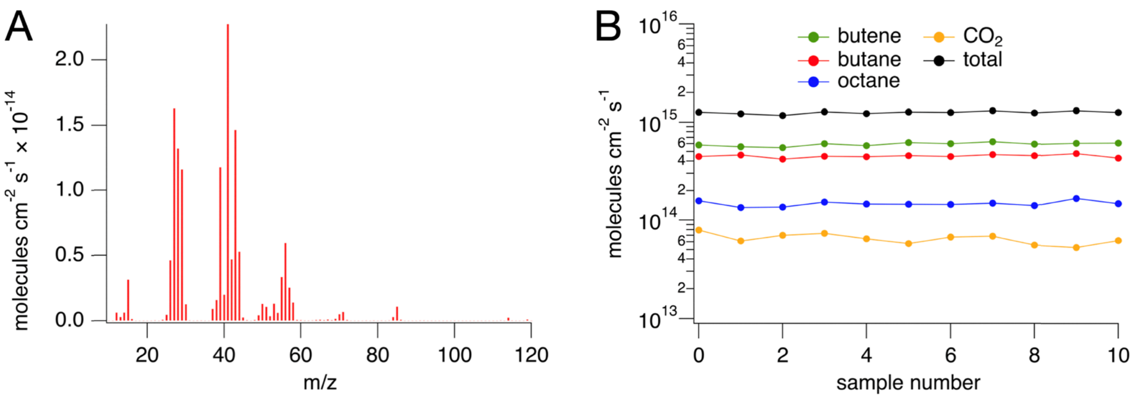

Fig. 5 (A) Outgassing mass spectrum of TinOH upon EUV irradiation. (B) Outgassing rates of different products during the experiment.

Table 1 Relative yields of octane, butane, butene and carbon dioxide upon EUV irradiation of tin–oxo cages. Standard deviation from 11 samples during one experimental run

Product	TinF	TinOH (run 1)	TinOH (run 2)
Butene	49 ± 5	40 ± 3	47 ± 1
Butane	34 ± 3	35 ± 2	36 ± 1
Octane	13 ± 1	20 ± 1	12 ± 1
CO_2	4.5 ± 0.4	5.4 ± 0.4	5.2 ± 0.6

spectra on the RGA. The accuracy of the relative peak heights in the NIST data is not specified, and one may expect different mass analyzers to have a different sensitivity curve (signal intensity *vs.* m/z value). The RGA used in the present work was calibrated in a study of EUV photoresists in which higher m/z values were of interest, and the extrapolation to the lower values in the present work may be inaccurate.[70]

We have considered other approaches to fitting the data, for example sequentially subtracting the contributions of octane, butane, butene and CO_2 from the total based on their unique peaks, or fitting only the range $m/z > 43$ in which the RGA calibration is more trustworthy, but in all cases we find that butane and butene are formed in similar amounts, octane is formed to a much lesser extent, and CO_2 is a minor product. The numerical data in Table 1 suggest that the yield of butene is larger than that of butane. The standard deviations, however, do not take systematic errors in the analysis into account, so we consider such a conclusion premature. To quantify the yields more accurately, calibration of the RGA with the proposed reaction products is required.

Comparing the data in Fig. S9 we note that the average total outgassing rate for TinOH is 2 times larger than that for TinF. This agrees with the lower sensitivity of TinF observed in the STXM experiments discussed above.

When comparing the two data sets of TinOH, we see differences that exceed the statistical errors and cannot be due to the systematic error introduced by the data analysis. In data set 1, the relative yield of octane is higher than in data set 2. It is known that TinOH undergoes ageing,[68] and the time between preparation of the films in Amsterdam and their exposure in Leuven in the two experiments was different. One experimentally confirmed source of ageing is the loss of co-crystallized isopropanol from the crystals;[71] another possible cause is the transfer of a proton from a bridging OH-group to the strongly basic counterion, observed in computational studies.[72] To prevent such proton transfer in quantum chemical models, we have included water molecules in them, which hydrogen bond to the OH^- in a manner similar to the isopropanol co-solvent in the crystal structure (see SI, Fig. S12).[64] From an experimental perspective we found it advantageous to use less reactive counterions such as acetate which gives rise to a similar patterning sensitivity as TinOH,[28,62] but appears less sensitive to ageing.

By focusing on a small number of ions rather than scanning the whole spectrum, the time evolution of the outgassing products can be monitored on a single spot with a resolution of 0.65 s per point. The relative intensities of the signals at m/z 84 (octane), 56 (butene), and 44 (CO_2) during the exposure of TinOH are shown in Fig. 6.

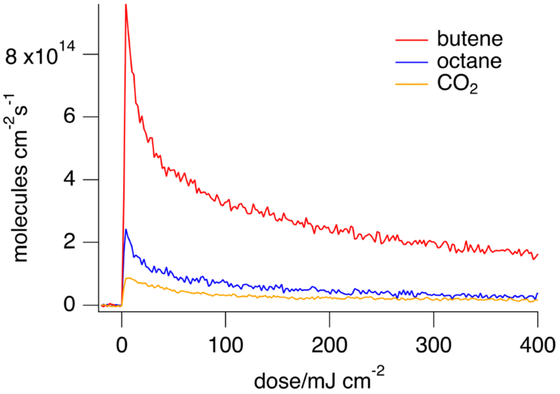

Fig. 6 Outgassing rates derived by monitoring selected ions during EUV exposure of a single spot on a film of TinOH.

Fig. 6 reveals that the rate of outgassing of butene and octane initially decreases sharply with increasing accumulated dose on the sample. If Sn–C bond cleavage occurred with a single rate constant, an exponential decrease of the reaction rate would be expected, but this is clearly not the case. The contribution of carbon dioxide (m/z 44) decreases over time, but more slowly than that of butene and octane. It remains uncertain whether CO_2 is a genuine EUV photoreaction product. Possibly, some CO_2 is bound to the pristine tin–oxo cage[32] and is eliminated after ionization, but CO_2 could also be a product of oxidation of minor contaminants. In any case, the amount of CO_2 detected is small compared to the main hydrocarbon products.

Film thickness changes upon EUV exposure

To determine how the thickness of the resist film changes with exposure dose upon EUV irradiation, 16 different spots on a TinOH-coated wafer were exposed to different doses up to 5400 mJ cm^{-2}. The initial thickness of the film at each spot, measured by means of ellipsometry before exposure, is shown in Fig. 7A in green. The corresponding thickness values measured at the same positions on the wafer after exposure are plotted in blue. The red points show the thickness of the same spots measured after the development of the exposed resist. The slope of this curve between the dose at which the onset of retention occurs (D_0 = 9 mJ cm^{-2}) and the dose at which maximum thickness is reached (D_{100} = 45 mJ cm^{-2}) is known as the contrast γ of the resist.[73] Here we find γ = 1.44. The values of D_0 and D_{100} agree with those reported by Haitjema *et al.* on the basis of AFM measurements.[28] The sensitivity of the photoresist is often described by the dose at which half of the maximum thickness is reached, $D_{50} \approx 20$ mJ cm^{-2}. For this type of resist the contrast and sensitivity can be enhanced by heating the film after exposure and before development.[28,68]

The difference between the original film thickness and the one after exposure reveals shrinkage due to the outgassing of the hydrocarbon products, which decreases the average size of

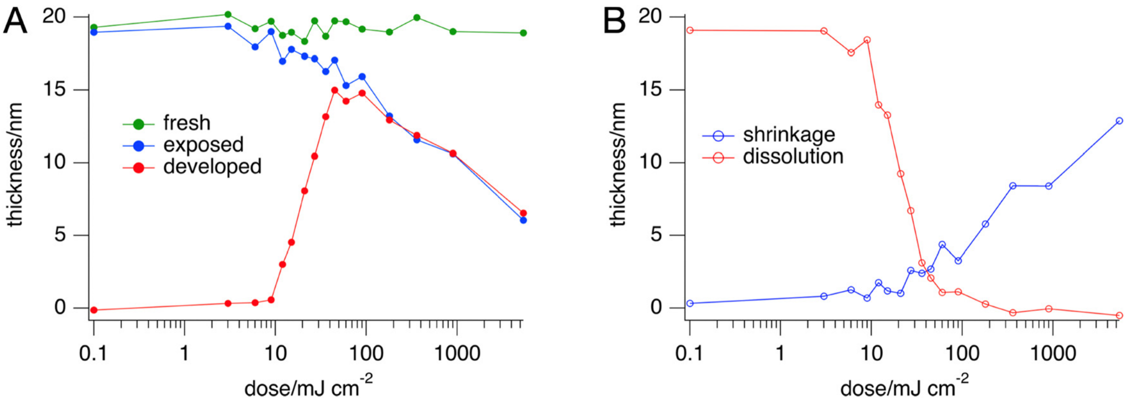

Fig. 7 (A) Thickness of the TinOH resist film measured at 16 different positions with different exposure doses, before exposing the wafer, after exposure to EUV, and after development. (B) Blue: thickness difference between the unexposed and exposed film. Red: difference between exposed and developed.

the resist molecules. Possibly, cross-linking between neighboring cage molecules also contributes to the shrinkage because bond formation reduces the distance between the tin–oxo cores. The difference in the film thickness after exposure and after development is due to dissolution of material during the development step. Shrinkage and dissolution are visualized in Fig. 7B.

Reaction mechanism

In earlier studies, ample evidence has been provided for tin–carbon bond cleavage as a key process upon activation of tin–oxo cages by photons or electrons.[29,60,62,64,66] In this work, we report the detection of the resulting hydrocarbon reaction products: butene, butane and octane. Recently, Dorney *et al.* reported similar experiments on TinOH and two other tin–oxo cage derivatives,[68] but they do not report (relative) yields, and do not mention the presence of butane. The three products may be formed by bimolecular reactions of the butyl radicals generated by Sn–C bond cleavage, as shown in steps (c) and (d) in Scheme 1.

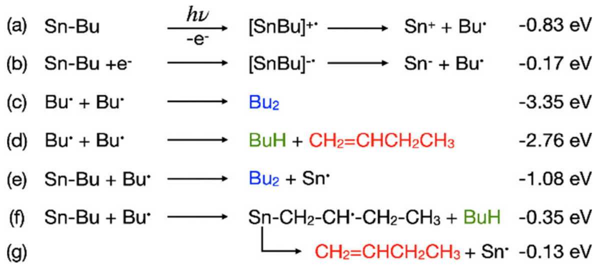

Scheme 1 Reaction scheme. Sn–Bu refers to the model of TinOH. (a) Photoionization and Sn–C bond breaking; (b) electron trapping on a tin–oxo cage and Sn–C bond breaking;[72] (c) radical combination to form octane; (d) radical disproportionation leading to butane and butene; (e) radical transfer leading to octane; (f) and (g) H-abstraction and bond cleavage leading to butane and butene with transfer of the radical site to Sn. Calculated reaction energies at the B3LYP/Def2TZVP//B3LYP/LANL2DZ level including zero-point vibrational energies. Details are in the SI (Fig. S12 and Table S3).

However, at the pressures in the exposure tool, $p \approx 10^{-9}$ mbar, the probability of encounter of two radicals is likely too low for bimolecular reactions to be effective. Moreover, the preferred reaction of two butyl radicals is combination (c) rather than disproportionation (d), in a ratio of 7 : 1,[74] but we find the opposite: butene and butane are the major products. Alternative pathways of formation of the closed shell products should be considered (Scheme 1). The butyl radical lost from an activated tin cage (step (a) or (b)) could react with an Sn–Bu unit in the same or another cage molecule, either by forming a C–C bond (step (e)) or by hydrogen abstraction (step (f)). Such reactions are thermodynamically favorable, because they exchange relatively weak Sn–C bonds for stronger C–H and C–C bonds. Note that they give rise to two (or more) Sn–C bond cleavages per ionization event, thus potentially doubling the quantum efficiency of the process. Moreover, the neutral tin-centered radical that can be formed in these processes is thermally labile. Bond dissociation energies of Sn–C bonds in closed-shell systems are ∼2.3 eV, but the loss of a butyl radical from the $Sn_{12}Bu_{11}$ radical requires only ∼1 eV because it is facilitated by a structural rearrangement of the cage structure.[66] It is known that the sensitivity and contrast of tin–oxo cage resists can be enhanced by post-exposure baking, and metastable radicals might be responsible for this.[28,75]

The X-ray absorption experiments above showed that the trifluoroacetate compound TinF is less EUV-sensitive than TinOH and the outgassing data agree with this. The outgassing product distribution of TinF is similar to that of TinOH, but the rates are smaller by a factor of 2. This indicates that the counterions play an important role in the mechanism of the solubility switching reaction. After photoionization, a covalent bond can be formed between the tin–oxo cage, now with a +3 charge, and the counterion.[62,66] Proton transfer to the counterion is another possible process.[72] The trifluoroacetate anion is less basic (pK_a 0.03)[76] and nucleophilic[77] than hydroxide (pK_a 14)[78] or acetate (pK_a 4.76).[79] This renders its reactions slower and less competitive with other processes (*e.g.* recombination of charges or radicals), which is a likely reason for the lower reactivity. Details of the computational results with some additional discussion are provided in the SI.

Quantum yield

When we assume that upon exposure the density of the material gradually increases from its initial value to that of the product of ultimate conversion, with the stoichiometry of Sn_2O_3,[80] we can use the observed thickness loss due to the decrease of molecular size as a measure of chemical conversion (see Fig. S11 for a graphical illustration). This is a reasonable approximation especially at small conversion. As explained in detail in the SI, the decrease in thickness of $\sim$2.7 nm at the dose needed for the maximum film retention (45 mJ cm^{-2}) corresponds to a loss of $\sim$2.2 butyl groups per tin cage. Based on the known absorption factor[33] α_{92eV} = 10.9 μm^{-1} and the initial film thickness, we calculate the number of photons absorbed, and we derive the quantum yield of the photochemical conversion as $\Phi \approx 3.3$ Sn–Bu bond breaking events per absorbed photon, averaged over the dose from 0 to 45 mJ cm^{-2}. However, as is apparent from Fig. 6, the reaction rate at the earliest stages of conversion is higher than the average and the initial quantum yield amounts to $\Phi \approx 5.4$.

Recent total electron yield measurements (TEY) on tin–oxo cage resists have shown that 3 to 4 electrons are generated per absorbed EUV photon.[81] Each electron leaves a hole behind, and both electrons and holes can undergo Sn–C bond cleavage (steps (a) and (b) in Scheme 1).[62] Thus, the TEY result suggests a maximum quantum yield of $\sim$7 Sn–C bond dissociations per absorbed photon. The quantum yield could be even higher if energy loss of the low-energy electrons leads to electronic excitation, or if radical fragmentation mechanisms such as those proposed in Scheme 1 occur. In practice, our results show that the quantum yield of conversion is much smaller than the theoretical maximum, which we attribute to various recombination processes.

In the XUV excitation energy range, the initial reaction quantum yield was estimated to be $\Phi \approx 1$ for TinOAc (tin–oxo cage with acetate counterions) which has a similar sensitivity as TinOH.[28] This number is consistent with the present result, because the number of electron–hole pairs created increases with the photon energy.[81] Also in the XUV range, the bond breaking quantum yield decreased sharply with conversion.

In 2017, Hinsberg and Meyers published the first simulation study of the solubility switching in a metal oxide EUV resist.[46] The simulation model did not feature an explicit molecular structure, but the presence of 12 ''metal–ligand'' bonds, and the activation mechanism based on metal–ligand bond breaking followed by cross-linking resembles that of tin–oxo cages. In the study, experimental data of an Inpria resist were used for calibration. The conversion was measured using infrared data, but details were not given. Like in our observations, the rate of conversion decreases with increasing conversion, but not as sharply. The experimental dose at which the film thickness after development is at its maximum (D_{100}) of $\sim$13 mJ cm^{-2} corresponds to $\sim$25% conversion. Hinsberg and Meyers did not disclose the chemical structure of the material for which the experimental data were obtained. The EUV absorption coefficient of the model was 16.6 μm^{-1}. In *n*-butyl tin–oxo cages the absorption coefficient is smaller, indicating that the Inpria model (if it is a dodecameric tin–oxo cage) must have a more compact organic shell, because the absorption at 92 eV originates mostly from tin atoms. From the simulations, Hinsberg and Meyers derived that 8 electrons are generated per photon, where they equate electrons generated with bond breaking reactions occurring. In other words, their data correspond with a bond-breaking quantum yield of Φ = 8. Similar quantum yields have been reported in more recent simulation studies.[47,50] Unfortunately, in these cases, even fewer calibration data were disclosed. In their seminal study of tin–oxo cages as EUV resists, Cardineau *et al.*[27] found that the sensitivity is enhanced when using weaker tin–alkyl bonds, *i.e.* with alkyl groups forming more stable radicals.

In a previous study from our laboratory, Haitjema *et al.* obtained the maximum retained thickness (after development) at an EUV dose D_{100} = 50 mJ cm^{-2} for TinOH and TinOAc films with an initial thickness of $\sim$40 nm and with no post-exposure bake applied to the films. They also observed a reduction in the thickness of the developed films for doses above 100 mJ cm^{-2}.[28] In the current study, the maximum retention of the resist film is reached at a similar dose of $\sim$45 mJ cm^{-2}. Further exposure leads to further hydrocarbon loss and densification, as is also apparent from the gradually increasing refractive indices derived from ellipsometry (Fig. S10B).

As shown in Fig. 7B, at a dose of $\sim$45 mJ cm^{-2}, the loss of material in the development step is already very small. However, with an average loss of $\sim$2.2 butyl groups per tin–oxo cage at this stage of conversion, it is not possible to form a highly cross-linked network. A substantial fraction of the tin–oxo cages may still be intact, but they are not removed by the developer. For a good understanding of how this type of photoresist works, more extensive studies of the development step are crucial.[49,82]

Conclusions

Extreme ultraviolet photo-induced chemical changes were studied in the *n*-butyltin–oxo cage materials TinOH and TinF. Both X-ray absorption and outgassing measurements showed that the former is $\sim$2 times more sensitive/reactive than the latter. No evidence was found for outgassing of tin species, neither for TinOH (Fig. 3) nor for TinF (Fig. 4B). This implies that contamination of the EUV lithography machine with tin from the photoresists is not likely to be a problem.

The outgassing reaction products were identified as predominantly 1-butene and *n*-butane, together with a smaller quantity of *n*-octane. These hydrocarbons result from the butyl radicals that originate from Sn–C bond breaking. The products are probably mostly formed inside the photoresist film, and a variety of possible reaction pathways may be involved in addition to simple disproportionation and C–C coupling of the radicals. Based on our results, we cannot exclude that other low molecular weight species are outgassing in smaller amounts.

Measurements of the thickness of TinOH films before exposure, after exposure, and after development show that the film thickness after development reaches a maximum of ∼85% of the original thickness at a dose of ∼45 mJ cm^{-2} (D_{100}). At this point, the development removes only very little material, and at higher doses the film shrinks further only due to outgassing. Using a simple model in which the shrinkage (prior to development) is assumed to be proportional to the loss of the volume of the organic fraction, we estimate that on average ∼2.2 butyl groups are lost per tin–oxo cage at D_{100}, with an average bond cleavage quantum yield of ∼3.3 Sn–C bonds per absorbed photon. The rate of outgassing of hydrocarbons, however, decreases sharply with conversion (Fig. 6), and the extrapolated quantum yield at zero conversion is ∼5.4. Considering the mechanism of activation *via* photoionization and secondary electron hole/pair generation, we can expect a quantum yield of at least 7 for the formation of reactive radical ion species. Reactions of the initially formed butyl radicals that lead to the closed-shell outgassing products inside the film further increase the maximum reaction quantum yield in terms of Sn–C bonds broken per absorbed photon.

Our study provides new (semi)quantitative insight into the EUV induced chemistry of tin–oxo cage photoresists that can be used to calibrate simulation models of EUV pattern formation. So far, models assume that all Sn–C bonds are equally reactive, and that the quantum yield does not change with conversion. This assumption has been shown to be incorrect.

Despite the progress made, many questions remain. Cross-linking between tin–oxo cages has been proposed from the beginning of the research in this field,[27] but experimental data on how exactly the cages are connected are still lacking.[83] Our results indicate that extensive 3D network formation is not required for the film to become insoluble. For the understanding of pattern formation, more insight into the development of the exposed resist is crucial. We have proposed molecular level structures of the reaction products of the first activation step, but the number of possible follow-up reactions is large, and this forms a challenge for a systematic exploration by means of quantum chemical methods.[62] On the experimental side, more powerful techniques are needed that are sensitive enough to handle the minute quantities of material in the thin films and give detailed structural information.

Author contributions

An overview of the author contributions is provided in the SI, Table S4.

Conflicts of interest

There are no conflicts to declare.

Data availability

Data for this article including raw experimental data and data files to reproduce the figures in the main text and supplementary information (SI) are available at https://doi.org/10.21942/uva.30651692. Supplementary information is available. See DOI: https://doi.org/10.1039/d5tc04167h.

Acknowledgements

Part of this work has been carried out at the Advanced Research Center for Nanolithography (ARCNL), a public–private partnership of the University of Amsterdam (UvA), the VU University Amsterdam (VU), the Netherlands Organisation for Scientific Research (NWO) and the semiconductor equipment manufacturer ASML. This work used the Dutch national e-infrastructure with the support of the SURF Cooperative using grants no. EINF-174, EINF-1911 and EINF-4039. K. W. received funding from the European Union's Horizon 2020 research and innovation program under the Marie Sklodowska-Curie grant agreement no. 701647. The PolLux end station was financed by the German Ministerium für Bildung und Forschung (BMBF) through ErUM-Pro contracts 05K16WED, 05K19WE2 and 05K22WE2. We thank the Paul Scherrer Institute for access to the PolLux beam line (proposals 20180709 and 20182195) and the XIL-II beam line (proposals 20180993 and 20182117). This project contributes to the ELENA (low energy ELEctron driven chemistry for the advantage of emerging NAno-fabrication method) European training network (ITN Marie Sklodowska-Curie Grant Agreement no. 722149 funded by European Union's Framework Programme for Research and Innovation Horizon 2020). It has received further funding from the EU-H2020 research and innovation program under grant agreement no. 654360 which provided part of the access to PSI within the framework of the Nanoscience Foundries and Fine Analysis Europe Transnational Access Activity. We thank Dr Sonia Castellanos for her help with the experiments and for her critical comments on the manuscript, and Dr Peter Kraus (ARCNL) for fruitful discussions.

Notes and references

1 IEEE International Roadmap for Devices and Systems, ''Lithography and Patterning'', Institute of Electrical and Electronics Engineers, 2024.
2 J. Miyazaki and A. Yen, EUV Lithography Technology for High-volume Production of Semiconductor Devices, *J. Photopolym. Sci. Technol.*, 2019, **32**, 195–201, DOI: 10.2494/photopolymer.32.195.
3 H. J. Levinson, High-NA EUV lithography: current status and outlook for the future, *Jpn. J. Appl. Phys.*, 2022, **61**, SD0803, DOI: 10.35848/1347-4065/ac49fa.
4 M. Neisser, N. G. Orji, H. J. Levinson, U. Celano, J. Moyne, S. Mashiro, D. Wilcox and S. Libman, How Lithography and Metrology Are Enabling Yield in the Next Generation of

Semiconductor Patterning, *Computer*, 2024, **57**, 51–58, DOI: 10.1109/mc.2023.3312767.

5 A. Lio, EUV Photoresists: A Progress Report and Future Prospects, *Synchrotron Radiat. News*, 2019, **32**, 9–14, DOI: 10.1080/08940886.2019.1634431.

6 T. Kozawa and S. Tagawa, Radiation Chemistry in Chemically Amplified Resists, *Jpn. J. Appl. Phys.*, 2010, **49**, 030001, DOI: 10.1143/JJAP.49.030001.

7 Q. Wang, Y. Zhou, X. Wang, H. Gao, Z. Shu, Z. Hu, P. Tao, Y. Ekinci, M. Vockenhuber, Y. Chen, H. Duan, H. Xu and X. He, Suppressing of secondary electron diffusion for high-precision nanofabrication, *Mater. Today*, 2023, **67**, 95–107, DOI: 10.1016/j.mattod.2023.06.005.

8 J. Torok, R. Del Re, H. Herbol, S. Das, I. Bocharova, A. Paolucci, L. E. Ocola, C. Ventrice Jr, E. Lifshin, G. Denbeaux and R. L. Brainard, Secondary Electrons in EUV Lithography, *J. Photopolym. Sci. Technol.*, 2013, **26**, 625–634, DOI: 10.2494/photopolymer.26.625.

9 H. Ito, Chemical amplification resists: inception, implementation in device manufacture, and new developments, *J. Polym. Sci., Part A: Polym. Chem.*, 2003, **41**, 3863–3870, DOI: 10.1002/pola.10963.

10 H. Ito, Chemical Amplification Resists for Microlithography. *Microlithography Molecular Imprinting: Advances in Polymer Science*, 2005, pp. 37–245.

11 D. P. Sanders, Advances in Patterning Materials for 193 nm Immersion Lithography, *Chem. Rev.*, 2010, **110**, 321–360, DOI: 10.1021/cr900244n.

12 R. Brainard, C. Higgins, E. Hassanein, R. Matyi and A. Wuest, Film quantum yields of ultrahigh PAG EUV photoresists, *J. Photopolym. Sci. Technol.*, 2008, **21**, 457–464, DOI: 10.2494/photopolymer.21.457.

13 R. Hirose, T. Kozawa, S. Tagawa, T. Kai and T. Shimokawa, Dependence of Acid Generation Efficiency on Molecular Structures of Acid Generators upon Exposure to Extreme Ultraviolet Radiation, *Appl. Phys. Expr.*, 2008, **1**, 027004, DOI: 10.1143/apex.1.027004.

14 C. D. Higgins, C. R. Szmanda, A. Antohe, G. Denbeaux, J. Georger and R. L. Brainard, Resolution, Line-Edge Roughness, Sensitivity Tradeoff, and Quantum Yield of High Photo Acid Generator Resists for Extreme Ultraviolet Lithography, *Jpn. J. Appl. Phys.*, 2011, **50**, 036504, DOI: 10.1143/jjap.50.036504.

15 R. P. Oleksak, R. E. Ruther, F. Luo, K. C. Fairley, S. R. Decker, W. F. Stickle, D. W. Johnson, E. L. Garfunkel, G. S. Herman and D. A. Keszler, Chemical and Structural Investigation of High-Resolution Patterning with HafSO$_x$, *ACS Appl. Mater. Interfaces*, 2014, **6**, 2917–2921, DOI: 10.1021/am405463u.

16 R. P. Oleksak, R. E. Ruther, F. Luo, J. M. Amador, S. R. Decker, M. N. Jackson, J. R. Motley, J. K. Stowers, D. W. Johnson, E. L. Garfunkel, D. A. Keszler and G. S. Herman, Evaluation of Thermal and Radiation Induced Chemistries of Metal Oxo–Hydroxo Clusters for Next-Generation Nanoscale Inorganic Resists, *ACS Appl. Nano Mater.*, 2018, **1**, 4548–4556, DOI: 10.1021/acsanm.8b00865.

17 J. Peter, M. G. Moinuddin, S. Ghosh, S. K. Sharma and K. E. Gonsalves, Organotin in Nonchemically Amplified Polymeric Hybrid Resist Imparts Better Resolution with Sensitivity for Next-Generation Lithography, *ACS Appl. Polym. Mater.*, 2020, **2**, 1790–1799, DOI: 10.1021/acsapm.0c00005.

18 S. Nandi, L. Khillare, M. G. Moinuddin, S. Kumar, M. Chauhan, S. K. Sharma, S. Ghosh and K. E. Gonsalves, Macrocycle Network-Aided Nanopatterning of Inorganic Resists on Silicon, *ACS Appl. Nano Mater.*, 2022, **5**, 10268–10279, DOI: 10.1021/acsanm.2c01321.

19 Z. Wang, X. Yao, H. An, Y. Wang, J. Chen, S. Wang, X. Guo, T. Yu, Y. Zeng, G. Yang and Y. Li, Recent Advances in Organic-inorganic Hybrid Photoresists, *J. Microelectron. Manuf.*, 2021, **4**, 21040101, DOI: 10.33079/jomm.21040101.

20 G. Lim, K. Lee, S. Choi and H. J. Yoon, Organometallic and coordinative photoresist materials for EUV lithography and related photolytic mechanisms, *Coord. Chem. Rev.*, 2023, **493**, 215307, DOI: 10.1016/j.ccr.2023.215307.

21 C. K. Ober, F. Käfer and C. Yuan, Recent developments in photoresists for extreme-ultraviolet lithography, *Polymer*, 2023, **280**, 126020, DOI: 10.1016/j.polymer.2023.126020.

22 T. Kozawa, Design strategy of extreme ultraviolet resists, *Jpn. J. Appl. Phys.*, 2024, **63**, 050101, DOI: 10.35848/1347-4065/ad3a4c.

23 Y. Si, D. Zhou, J. Zhao, Y. Peng, P. Chen, J. Fan and X. Peng, Radiation chemistry of a novel zinc–oxo cluster crosslinking strategy for EUV patterning, *Sci. China Mater.*, 2024, **67**, 1588–1593, DOI: 10.1007/s40843-023-2827-8.

24 R.-S. Zhang, L. Miao, X.-Y. Lu, Q. Li, F. Luo, H.-Y. Qiu and G.-P. Wu, Norbornene and Epoxide-Substituted Silsesquioxane Photoresists with High-Sensitivity and Stability, *ACS-Nano*, 2025, **19**, 38243–38254, DOI: 10.1021/acsnano.5c06472.

25 R. Zhou, M. Cao, Y. Tan, M. Neisser and H. Xu, Polytelluoxane as the ideal formulation for EUV photoresist, *Sci. Adv.*, 2025, **11**, eadx1918, DOI: 10.1126/sciadv.adx1918.

26 R. Fallica, J. K. Stowers, A. Grenville, A. Frommhold, A. P. G. Robinson and Y. Ekinci, Dynamic absorption coefficients of chemically amplified resists and nonchemically amplified resists at extreme ultraviolet, *J. Micro/Nanolithogr., MEMS, MOEMS*, 2016, **15**, 033506, DOI: 10.1117/1.JMM.15.3.033506.

27 B. Cardineau, R. Del Re, M. Marnell, H. Al-Mashat, M. Vockenhuber, Y. Ekinci, C. Sarma, D. A. Freedman and R. L. Brainard, Photolithographic properties of tin-oxo clusters using extreme ultraviolet light (13.5 nm), *Microelectron. Eng.*, 2014, **127**, 44–50, DOI: 10.1016/j.mee.2014.04.024.

28 J. Haitjema, Y. Zhang, M. Vockenhuber, D. Kazazis, Y. Ekinci and A. M. Brouwer, Extreme ultraviolet patterning of tin-oxo cages, *J. Micro/Nanolithogr., MEMS, MOEMS*, 2017, **16**, 033510, DOI: 10.1117/1.JMM.16.3.033510.

29 Y. Zhang, J. Haitjema, X. Liu, F. Johansson, A. Lindblad, S. Castellanos, N. Ottosson and A. M. Brouwer, Photochemical conversion of tin-oxo cage compounds studied using hard X-ray photoelectron spectroscopy, *J. Micro/Nanolithogr.,*

MEMS, MOEMS, 2017, **16**, 023510, DOI: 10.1117/1.JMM.16.2.023510.

30 R. T. Frederick, S. Saha, J. T. Diulus, F. Luo, J. M. Amador, M. Li, D.-H. Park, E. L. Garfunkel, D. A. Keszler and G. S. Herman, Thermal and radiation chemistry of butyltin oxo hydroxo: a model inorganic photoresist, *Microelectron. Eng.*, 2019, **205**, 26–31, DOI: 10.1016/j.mee.2018.11.011.

31 N. Kenane, M. A. Grove, C. K. Perkins, T. R. Reynolds, P. H. Cheong and D. A. Keszler, Hydrolysis and Condensation of *n*-BuSnCl$_3$: Enabling Deposition of Smooth Metal Oxide Photoresist Thin Films, *Inorg. Chem.*, 2020, **59**, 3934–3941, DOI: 10.1021/acs.inorgchem.9b03589.

32 N. Kenane and D. A. Keszler, High-Resolution Lithographic Patterning with Organotin Films: Role of CO$_2$ in Differential Dissolution Rates, *ACS Appl. Mater. Interfaces*, 2021, **13**, 18974–18983, DOI: 10.1021/acsami.0c21942.

33 R. Fallica, J. Haitjema, L. Wu, S. Castellanos, A. M. Brouwer and Y. Ekinci, Absorption coefficient of metal-containing photoresists in the extreme ultraviolet, *J. Micro/Nanolithogr., MEMS, MOEMS*, 2018, **17**, 023505, DOI: 10.1117/1.JMM.17.2.023505.

34 S. Castellanos, L. Wu, M. Baljozovic, G. Portale, D. Kazazis, M. Vockenhuber, Y. Ekinci and T. A. Jung, Ti, Zr, and Hf-based molecular hybrid materials as EUV photoresists, *Proc. SPIE*, 2018, **10583**, 10583A, DOI: 10.1117/12.2297167.

35 L. Wu, M. Baljozovic, G. Portale, D. Kazazis, M. Vockenhuber, T. Jung, Y. Ekinci and S. Castellanos, Mechanistic insights in Zr-and Hf-based molecular hybrid EUV photoresists, *J. Micro/Nanolithogr., MEMS, MOEMS*, 2019, **18**, 013504, DOI: 10.1117/1.JMM.18.1.013504.

36 L. Wu, M. Tiekink, A. Giuliani, L. Nahon and S. Castellanos, Tuning photoionization mechanisms of molecular hybrid materials for EUV lithography applications, *J. Mater. Chem. C*, 2019, **7**, 33–37, DOI: 10.1039/c8tc05273e.

37 N. Thakur, M. Vockenhuber, Y. Ekinci and S. Castellanos, Zinc-based metal oxoclusters: towards enhanced EUV absorptivity, *Proc. SPIE*, 2019, **10957**, 109570D, DOI: 10.1117/12.2514814.

38 L. Wu, I. Bespalov, K. Witte, O. Lugier, J. Haitjema, M. Vockenhuber, Y. Ekinci, B. Watts, A. M. Brouwer and S. Castellanos, Unravelling the effect of fluorinated ligands in hybrid EUV photoresists by X-ray spectroscopy, *J. Mater. Chem. C*, 2020, **8**, 14757–14765, DOI: 10.1039/d0tc03216f.

39 A. M. Brouwer, Chemical Mechanisms of Metal-Based Extreme Ultraviolet Resists, *J. Photopolym. Sci. Technol.*, 2022, **35**, 81–86, DOI: 10.2494/photopolymer.35.81.

40 N. Thakur, M. Vockenhuber, Y. Ekinci, B. Watts, A. Giglia, N. Mahne, S. Nannarone, S. Castellanos and A. M. Brouwer, Fluorine-Rich Zinc Oxoclusters as Extreme Ultraviolet Photoresists: Chemical Reactions and Lithography Performance, *ACS Mater. Au*, 2022, **2**, 343–355, DOI: 10.1021/acsmaterialsau.1c00059.

41 E. C. Mattson, S. M. Rupich, Y. Cabrera and Y. J. Chabal, Role of excess ligand and effect of thermal treatment in hybrid inorganic–organic EUV resists, *Proc. SPIE*, 2018, **10583**, 1058309, DOI: 10.1117/12.2300064.

42 Q. Evrard, N. Sadegh, S. Mathew, E. Zuidinga, B. Watts, M. Paradiz Dominguez, A. Giglia, N. Mahne, S. Nannarone, A. Nishimura, T. Goya, T. Sugioka, M. Vockenhuber, Y. Ekinci and A. M. Brouwer, Extreme Ultraviolet Photoresponse of Organotin-Based Photoresists with Borate Counteranions, *ACS Appl. Mater. Interfaces*, 2024, **16**, 42947–42956, DOI: 10.1021/acsami.4c08636.

43 R. T. Frederick, J. T. Diulus, D. C. Hutchison, M. R. Olsen, I. Lyubinetsky, M. Nyman and G. S. Herman, Surface characterization of tin-based inorganic EUV resists, *Proc. SPIE*, 2018, **10586**, 1058607, DOI: 10.1117/12.2297484.

44 G. Kim, Y. Ku, S. Jeon, J. Lee, S. Lee, B. J. Jung, S. Lee, C. Ryu, K. Park, Y. L. Jung, C. Jeong and J. Choi, Tin-Oxo Nanocluster Composite Films as Positive-Tone Photoresist for Extreme UV Lithography, *Adv. Funct. Mater.*, 2025, **35**, 2503002, DOI: 10.1002/adfm.202503002.

45 D. P. Singh, L. Galleni, F. S. Sajjadian, I. Pollentier, F. Holzmeier, G. Pourtois, S. De Gendt, M. J. van Setten, T. Conard, J. S. Petersen, P. A. W. van der Heide and K. M. Dorney, Resolving In Situ Exposure Dynamics in a Chemically Amplified EUV Photoresist Using Table-Top EUV Photoemission Spectroscopy, *ACS Appl. Mater. Interfaces*, 2025, **17**, 52567–52579, DOI: 10.1021/acsami.5c09589.

46 W. D. Hinsberg and S. Meyers, A numeric model for the imaging mechanism of metal oxide EUV resists, *Proc. SPIE*, 2017, **10146**, 1014604, DOI: 10.1117/12.2260265.

47 R. Maas, M.-C. van Lare, G. Rispens and S. F. Wuister, Stochastics in extreme ultraviolet lithography: investigating the role of microscopic resist properties for metal-oxide-based resists, *J. Micro/Nanolithogr., MEMS, MOEMS*, 2018, **17**, 041003, DOI: 10.1117/1.jmm.17.4.041003.

48 C. D. Needham, A. Narasimhan, U. Welling, L. S. Melvin III, P. De Schepper, J. Wouters, J. Severi, D. De Simone and S. Meyers, Calibration of a MOx-specific EUV photoresist lithography model, *Proc. SPIE*, 2020, **11323**, 113230G.

49 Z. Belete, P. De Bisschop, U. Welling and A. Erdmann, Stochastic simulation and calibration of organometallic photoresists for extreme ultraviolet lithography, *J. Micro/Nanopattern. Mater. Metrol.*, 2021, **20**, 014801, DOI: 10.1117/1.jmm.20.1.014801.

50 E. C. Hansen, Y. Zhang, J. Y. Kim and W. D. Hinsberg, Analytical approach to metal oxide resist modeling: exposure, bake, and network formation, *J. Micro/Nanopattern. Mater. Metrol.*, 2022, **21**, 041405, DOI: 10.1117/1.jmm.21.4.041405.

51 L. Fernández Míguez, P. A. Bobbert and R. Coehoorn, Molecular-scale kinetic Monte Carlo simulation of pattern formation in photoresist materials for EUV nanolithography, *J. Appl. Phys.*, 2024, **136**, 0235702, DOI: 10.1063/5.0239120.

52 C. D. Needham, U. Welling, A. K. Narasimhan, P. De Schepper, L. McQuade, M. Kocsis, L. S. Melvin, J. K. Stowers and S. T. Meyers, Advanced simulations using an improved metal oxide photoresist model, *Proc. SPIE*, 2024, **12957**, 129571, DOI: 10.1117/12.3010941.

53 C. Eychenne-Baron, F. Ribot and C. Sanchez, New synthesis of the nanobuilding block $\{(\mathrm{BuSn})_{12}\mathrm{O}_{14}(\mathrm{OH})_6\}^{2+}$and exchange properties of $\{(\mathrm{BuSn})_{12}\mathrm{O}_{14}(\mathrm{OH})_6\}(\mathrm{O}_3\mathrm{SC}_6\mathrm{H}_4\mathrm{CH}_3)_2$,

J. Organomet. Chem., 1998, **567**, 137–142, DOI: 10.1016/S0022-328X(98)00676-7.

54 L. Van Lokeren, R. Willem, D. van der Beek, P. Davidson, G. A. Morris and F. Ribot, Probing the Anions Mediated Associative Behavior of Tin-12 Oxo-Macrocations by Pulsed Field Gradient NMR Spectroscopy, *J. Phys. Chem. C*, 2010, **114**, 16087–16091, DOI: 10.1021/jp100709j.

55 Y. Zhang, J. Haitjema, S. Castellanos, O. Lugier, N. Sadegh, R. Ovsyannikov, E. Giangrisostomi, F. O. L. Johansson, E. Berggren, A. Lindblad and A. M. Brouwer, Extreme ultraviolet photoemission of a tin-based photoresist, *Appl. Phys. Lett.*, 2021, **118**, 171903, DOI: 10.1063/5.0047269.

56 N. Mojarad, J. Gobrecht and Y. Ekinci, Interference lithography at EUV and soft X-ray wavelengths: principles, methods, and applications, *Microelectron. Eng.*, 2015, **143**, 55–63, DOI: 10.1016/j.mee.2015.03.047.

57 J. Raabe, G. Tzvetkov, U. Flechsig, M. Böge, A. Jaggi, B. Sarafimov, M. G. Vernooij, T. Huthwelker, H. Ade, D. Kilcoyne, T. Tyliszczak, R. H. Fink and C. Quitmann, PolLux: a new facility for soft X-ray spectromicroscopy at the Swiss Light Source, *Rev. Sci. Instrum.*, 2008, **79**, 113704, DOI: 10.1063/1.3021472.

58 I. Pollentier, G. Aksenov, A. M. Goethals, R. Gronheid, R. Jonckheere and M. Leeson, Measurement and analysis of EUV photoresist related outgassing and contamination, *Proc. SPIE*, 2009, **7271**, 727146, DOI: 10.1117/12.814862.

59 B. L. Henke, E. M. Gullikson and J. C. Davis, X-ray interactions: photoabsorption, scattering, transmission and reflection at $E = 50$–30 000 eV, $Z = 1$-92, *At. Data Nucl. Data Tables*, 1993, **55**, 181–342, DOI: 10.1006/adnd.1993.1013.

60 J. Haitjema, S. Castellanos, O. Lugier, I. Bespalov, R. Lindblad, M. Timm, C. Bülow, V. Zamudio-Bayer, J. T. Lau, B. von Issendorff, R. Hoekstra, K. Witte, B. Watts, T. Schlathölter and A. M. Brouwer, Soft X-Ray Absorption and Fragmentation of Tin-oxo Cage Photoresists, *Phys. Chem. Chem. Phys.*, 2024, **26**, 5986–5998, DOI: 10.1039/d3cp05428d.

61 https://henke.lbl.gov/optical_constants/, accessed June 21, 2024.

62 N. Sadegh, Q. Evrard, P. M. Kraus and A. M. Brouwer, XUV Absorption Spectroscopy and Photoconversion of a Tin-oxo Cage Photoresist, *J. Phys. Chem. C*, 2024, **128**, 3965–3974, DOI: 10.1021/acs.jpcc.3c07480.

63 M. C. Sharps, R. T. Frederick, M. L. Javitz, G. S. Herman, D. W. Johnson and J. E. Hutchison, Organotin Carboxylate Reagents for Nanopatterning: Chemical Transformations during Direct-Write Electron Beam Processes, *Chem. Mater.*, 2019, **31**, 4840–4850, DOI: 10.1021/acs.chemmater.9b01440.

64 I. Bespalov, Y. Zhang, J. Haitjema, R. M. Tromp, S. J. van der Molen, A. M. Brouwer, J. Jobst and S. Castellanos, Key Role of Very Low Energy Electrons in Tin-based Molecular Resists for Extreme Ultraviolet Nanolithography, *ACS Appl. Mater. Interfaces*, 2020, **12**, 9881–9889, DOI: 10.1021/acsami.9b19004.

65 J. T. Diulus, R. T. Frederick, D. C. Hutchison, I. Lyubinetsky, R. Addou, M. Nyman and G. S. Herman, Effect of Ambient Conditions on Radiation-Induced Chemistries of a Nanocluster Organotin Photoresist for Next-Generation EUV Nanolithography, *ACS Appl. Nano Mater.*, 2020, **3**, 2266–2277, DOI: 10.1021/acsanm.9b02387.

66 J. Haitjema, L. Wu, A. Giuliani, L. Nahon, S. Castellanos and A. M. Brouwer, UV and VUV-induced fragmentation of tin-oxo cage ions, *Phys. Chem. Chem. Phys.*, 2021, **23**, 20909–20918, DOI: 10.1039/D1CP03148A.

67 P. J. Linstrom and W. G. Mallard, The NIST Chemistry WebBook: a chemical data resource on the internet, *J. Chem. Eng. Data*, 2001, **46**, 1059–1063, DOI: 10.1021/je000236i.

68 K. M. Dorney, I. Pollentier, F. Holzmeier, R. Fallica, Y.-L. Chen, L. Piatti, D. P. Singh, L. Galleni, M. J. van Setten, H. S. Suh, D. De Simone, G. Pourtois, P. A. W. van der Heide and J. Petersen, Fundamental understanding of exposure and process chemistry for enhanced lithography and stability of metal oxide resists, *Proc. SPIE*, 2025, **13428**, 134281C, DOI: 10.1117/12.3051260.

69 S. Stein, Mass spectral reference libraries: an ever-expanding resource for chemical identification, *Anal. Chem.*, 2012, **84**, 7274–7282, DOI: 10.1021/ac301205z.

70 I. Pollentier, R. Lokasani, R. Gronheid, S. Hill, C. Tarrio and T. Lucatorto, Relationship between resist related outgassing and witness sample contamination in the NXE outgas qualification using electrons and EUV, *Proc. SPIE*, 2013, **8679**, 86790K, DOI: 10.1117/12.2011541.

71 F. Banse, F. Ribot, P. Tolédano, J. Maquet and C. Sanchez, Hydrolysis of Monobutyltin Trialkoxides: Synthesis and Characterizations of $\{(BuSn)_{12}O_{14}(OH)_6\}(OH)_2$, *Inorg. Chem.*, 1995, **34**, 6371–6379, DOI: 10.1021/ic00129a023.

72 J. H. Ma, C. Needham, H. Wang, A. Neureuther, D. Prendergast and P. Naulleau, Mechanistic Advantages of Organotin Molecular EUV Photoresists, *ACS Appl. Mater. Interfaces*, 2022, **14**, 5514–5524, DOI: 10.1021/acsami.1c12411.

73 R. G. Jones, C. K. Ober, T. Hayakawa, C. K. Luscombe and N. Stingelin, Terminology of polymers in advanced lithography (IUPAC Recommendations 2020), *Pure Appl. Chem.*, 2020, **92**, 1861–1891, DOI: 10.1515/pac-2018-1215.

74 W. E. Morganroth and J. G. Calvert, The Photolysis of 1,1′-Azo-*n*-butane Vapor. The Reactions of the *n*-Butyl Free Radical, *J. Am. Chem. Soc.*, 1966, **88**, 5387–5392, DOI: 10.1021/ja00975a004.

75 S. Castellanos, P. De Schepper, M. Bhattacharya, J. Doise, J. Wouters, A. K. Narasimhan, B. Cardineau, L. McQuade, C. D. Needham, M. Kocsis, K. Kasahara and S. T. Meyers, EUV metal oxide resists: impact of the environment composition on CD during post-exposure delay, *Proc. SPIE*, 2024, **12957**, 1295707, DOI: 10.1117/12.3010921.

76 D. Balasuryia, A. Queral-Beltran, T. Vick, S. Simpson, S. Lacorte, D. S. Aga and A. C. Hoepker, Experimental Determination of pK_a for 10 PFAS, Mono-, Di-, and Trifluoroacetic Acid by 19F-NMR, *Environ. Sci. Technol. Lett.*, 2025, **12**, 1238–1246, DOI: 10.1021/acs.estlett.5c00688.

77 C. G. Swain and C. B. Scott, Quantitative Correlation of Relative Rates. Comparison of Hydroxide Ion with Other

Nucleophilic Reagents toward Alkyl Halides, Esters, Epoxides and Acyl Halides1, *J. Am. Chem. Soc.*, 1953, **75**, 141–147, DOI: 10.1021/ja01097a041.

78 T. L. Neils, S. Schaertel and T. P. Silverstein, The pK_a of Water and the Fundamental Laws Describing Solution Equilibria: An Appeal for a Consistent Thermodynamic Pedagogy, *Helv. Chim. Acta*, 2024, **107**, 3, DOI: 10.1002/hlca.202400103.

79 R. N. Goldberg, N. Kishore and R. M. Lennen, Thermodynamic Quantities for the Ionization Reactions of Buffers, *J. Phys. Chem. Ref. Data*, 2002, **31**, 231–370, DOI: 10.1063/1.1416902.

80 G. Murken and M. Trömel, Uber das bei der Disproportionierung von SnO entstehende Zinnoxid, Sn_2O_3, *Z. Anorg. Allg. Chem.*, 1973, **397**, 117–126, DOI: 10.1002/zaac.19733970204.

81 N. Sadegh, Q. Evrard, N. Mahne, A. Giglia, S. Nannarone and A. M. Brouwer, Electron Generation in Tin-oxo Cage Extreme Ultraviolet Photoresists, *J. Photopolym. Sci. Technol.*, 2023, **36**, 373–378, DOI: 10.2494/photopolymer.36.373.

82 M. Kim, J. Moon, S. Park and M. Cho, Selective Dissolution Resistance Control of EUV Photoresist Using Multiscale Simulation: Rational Design of Hybrid System, *Macromolecules*, 2020, **53**, 4748–4763, DOI: 10.1021/acs.macromol.9b02378.

83 F.-L. Yang, Z.-B. Ye, D. Yang, M.-H. Wang, Y.-Q. Chen, P.-P. Zhou and F.-J. Gou, DFT Study on CO_2- and H_2O-Enhanced Solubility Contrast in Tin-Oxo Cage Photoresists, *Langmuir*, 2025, **41**, 26565–26574, DOI: 10.1021/acs.langmuir.5c02055.